NANO · MICRO small
www.small-journal.com

Phase Transition of $MoTe_2$ Controlled in van der Waals Heterostructure Nanoelectromechanical Systems

*Fan Ye, Arnob Islam, Yanan Wang, Jing Guo, and Philip X.-L. Feng**

This work reports experimental demonstrations of reversible crystalline phase transition in ultrathin molybdenum ditelluride ($MoTe_2$) controlled by thermal and mechanical mechanisms on the van der Waals (vdW) nanoelectromechanical systems (NEMS) platform, with hexagonal boron nitride encapsulated $MoTe_2$ structure residing on top of graphene layer. Benefiting from very efficient electrothermal heating and straining effects in the suspended vdW heterostructures, $MoTe_2$ phase transition is triggered by rising temperature and strain level. Raman spectroscopy monitors the $MoTe_2$ crystalline phase signatures in situ and clearly records reversible phase transitions between hexagonal 2H (semiconducting) and monoclinic 1T′ (metallic) phases. Combined with Raman thermometry, precisely measured nanomechanical resonances of the vdW devices enable the determination and monitoring of the strain variations as temperature is being regulated by electrothermal control. These results not only deepen the understanding of $MoTe_2$ phase transition, but also demonstrate a novel platform for engineering $MoTe_2$ phase transition and multiphysical devices.

1. Introduction

Phase transition (or phase change) devices, which operate via exploiting salient differences in electronic and photonic properties between two phases, have been emerging as attractive and exquisite platforms for scalable and energy-efficient memory and information processing applications.[1–4] Compared with traditional flash-based memory, phase change memory exhibits remarkable metrics, including superior endurance,[5] excellent data retention,[6] ultrafast write, and read speed.[7] For example, $Ge_2Sb_2Te_5$ (GST) phase-change memory exhibits 10^9 cycles endurance,[5] ten-year data retention in 300 to 500 K temperature range,[6] and sub-ten nanosecond switching speed.[7] These encouraging attainments make GST widely used in CDs, DVDs, and Blu-ray discs.[8] Besides memory applications, the fast switching and high endurance also make phase transition devices important components in neuromorphic computing hardware such as artificial synapses[9] and artificial neurons.[10] For instance, chalcogenide-based phase transition devices, which undergo phase transitions at nanoseconds timescale, have engendered integrate-and-fire functions as artificial neurons with both deterministic and stochastic dynamics.[10] These have played significant roles and witnessed promising advances in enabling state-of-the-art phase transition devices in modern and emerging technologies.

The advent of atomically thin layered crystals and 2D semiconductors (e.g., transition metal dichalcogenides, i.e., TMDCs)[11–13] offers exciting opportunities for novel nanoscale phase transition devices. Compared with traditional phase transition materials often having one amorphous phase and one crystalline phase, most 2D TMDC materials own two stable crystalline phases: 2H hexagonal phase and 1T′ monoclinic phase. In general, 2H phase TMDCs are endowed with bandgaps in their band structures and thus have been widely employed as channel materials for field-effect transistors (FETs). In contrast, 1T′ phase TMDCs exhibit metallic band structures without bandgap, thus offering low contact resistances with metals. Among the family of TMDCs, $MoTe_2$ has the lowest energy barrier between 2H phase and 1T′ phase (0.04 eV per $MoTe_2$ unit)[14,15] and thus it is regarded as the most promising candidate for 2D phase transition devices. In experiments, $MoTe_2$ phase transition has been realized by global heating with local strain applied from atomic force microscope (AFM),[16] laser heating,[17,18] mechanical strain-induced from ferroelectric substrates,[19] and electrostatic doping.[20] However, several deficiencies exist in these approaches. For example, the laser irradiation method continues to "sputter" $MoTe_2$ layer by layer and the remaining $MoTe_2$ sample permanently stays at 1T′ phase. Besides, the electrostatic doping approach inputs energy to 2H $MoTe_2$ with ionic liquids to realize phase transition, which makes it challenging to be integrated into CMOS for memory and computing applications. Therefore, novel reversible schemes and control of $MoTe_2$ phase transition on CMOS-friendly platforms are highly desirable and needed.

In this work, we describe the first experimental demonstration of controllable $MoTe_2$ phase transition directly on free-standing device platforms of van der Waals (vdW) heterostructure

F. Ye, A. Islam, Y. Wang, P. X.-L. Feng
Department of Electrical Engineering & Computer Science
Case School of Engineering
Case Western Reserve University
Cleveland OH 44106, USA
Y. Wang, J. Guo, P. X.-L. Feng
Department of Electrical & Computer Engineering
Herbert Wertheim College of Engineering
University of Florida
Gainesville FL 32611, USA
E-mail: philip.feng@ufl.edu
The ORCID identification number(s) for the author(s) of this article can be found under https://doi.org/10.1002/smll.202205327.

DOI: 10.1002/smll.202205327

nanoelectromechanical systems (NEMS). We fabricate suspended graphene/h-BN/$MoTe_2$/h-BN (Gr/h-BN/$MoTe_2$/h-BN) vdW heterostructures and investigate the phase transition behavior of $MoTe_2$. We conveniently use the DC bias voltage (V_{DC}) to electrothermally heat up the suspended graphene that serves as a nanoscale hotplate. As the temperature of graphene increases, the heat propagates to the upper layers and the temperature of the $MoTe_2$ flake increases. As the temperature rises, the tension level of the whole suspended vdW heterostructure membrane increases due to the negative thermal expansion coefficients (TECs) from both hexagonal boron nitride (h-BN) and graphene. As the applied voltage V_{DC} gradually increases, we observe clear, controllable, and reversible phase transitions between 2H phase and 1T′ phase. After the $MoTe_2$ fully converts to 1T′ phase, we gradually decrease the applied voltage and the $MoTe_2$ changes back to 2H phase. With solid experiments and comprehensive clarifying results, this work demonstrates a novel platform for building $MoTe_2$ phase transition nanoelectronic devices, toward future integration of phase-change random access memory and artificial neurons with tunable NEMS platforms.

2. Results and Discussions

Figure 1a illustrates the scheme of Gr/h-BN/$MoTe_2$/h-BN (counting from the bottom to top according to stacking during fabrication) vdW heterostructure nanoelectromechanical resonators with electrothermal excitation and tuning. The Gr/h-BN/$MoTe_2$/h-BN vdW heterostructure device is fabricated using the all-dry transfer method.[21] The graphene flake is first exfoliated on PDMS stamp and transferred onto pre-patterned substrates, followed by the transferring and stacking of h-BN, $MoTe_2$, and h-BN, consecutively. The optical microscopy image of the Gr/h-BN/$MoTe_2$/h-BN vdW heterostructure resonator is shown in

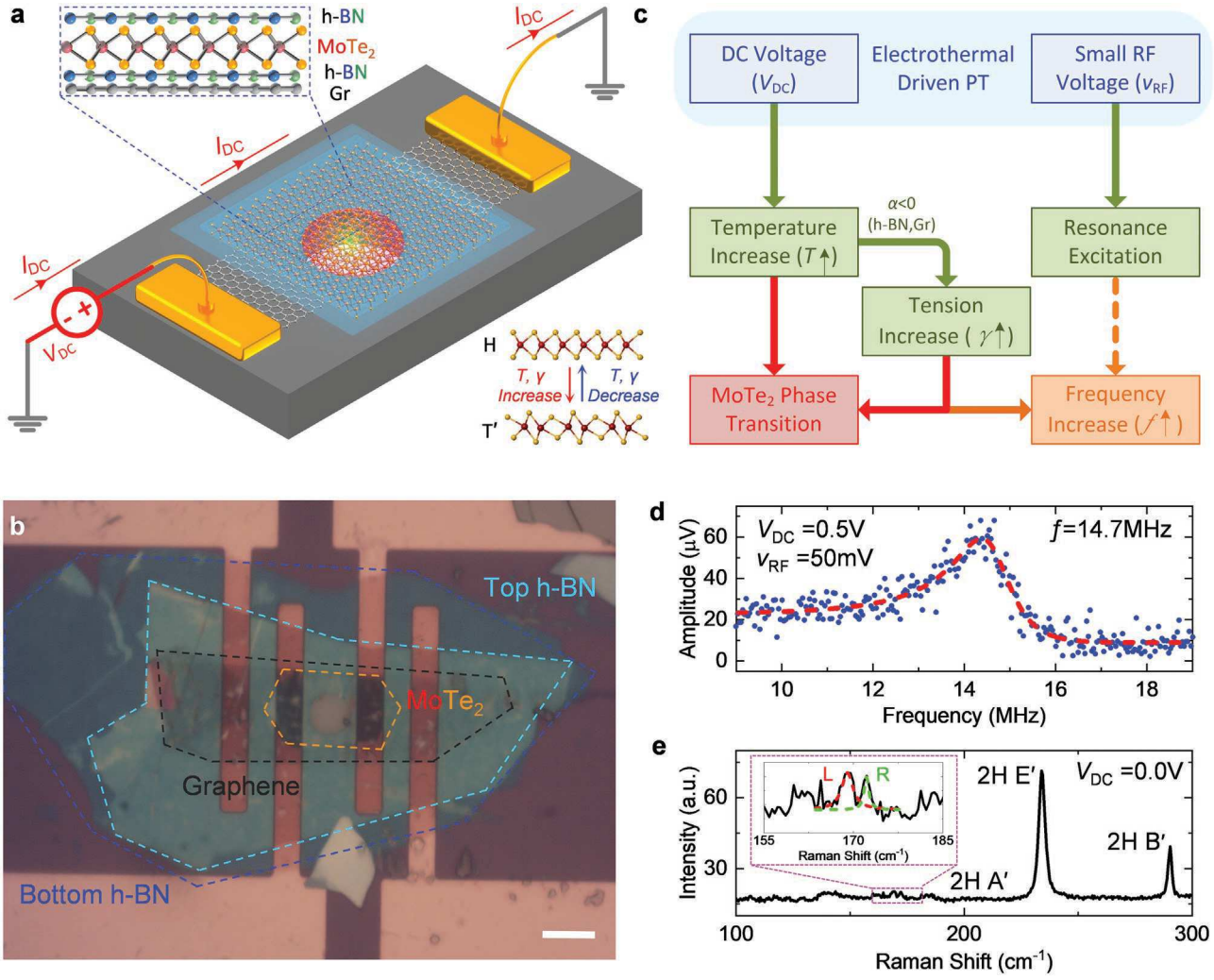

Figure 1. Graphene/h-BN/$MoTe_2$/h-BN van der Waals (vdW) heterostructure nanoelectromechanical resonators. a) Illustration of a circular drumhead graphene/h-BN/$MoTe_2$/h-BN resonator on a pre-patterned substrate. (upper left inset: cross-section view of the vdW heterostructure; bottom right inset: crystal structure of $MoTe_2$). b) Optical microscopy image of a graphene/h-BN/$MoTe_2$/h-BN vdW heterostructure nanoelectromechanical resonator. c) Analysis of coupling effects and signal transduction mechanisms of the vdW heterostructure resonators under Joule heating, for controlling the phase transition (PT). d) Fundamental-mode resonance of the vdW heterostructure in (b). e) $MoTe_2$ Raman signatures measured from the suspended region in (b) (inset: zoom-in figure of 2H peak A′). Scale bar: 10 μm.

Figure 1b. The few-layer graphene flake (black dashed lines) is first transferred onto the substrate, followed by another few-layer h-BN flake (outer blue dashed lines) stacking on top of the graphene. The bottom h-BN layer on top of graphene is used to provide electrical isolation for $MoTe_2$ from graphene. A few-layer $MoTe_2$ flake (orange dashed lines) is then transferred on top of the bottom h-BN. Finally, another few-layer h-BN (inner blue dashed lines) is stacked to cover the $MoTe_2$ to avoid environmental degradation and $MoTe_2$ sublimation at high temperatures.[16] All the devices are fabricated on a pre-patterned substrate with a circular drumhead microcavity (diameter ≈7.4 μm and a trench depth 2200 nm). After the device fabrication, the suspended vdW heterostructure is electrothermally heated up by a DC current from drain to source. In the meantime, a small RF voltage (ν_{RF}) is applied to excite the resonance. The small RF voltage gives rise to a small temperature vibration periodically, which generates a periodical thermal force on the vdW heterostructure. As the DC voltage (V_{DC}) increases, several effects are coupled together to trigger the phase transition (Figure 1c). First, due to the electrothermal effect, the heat propagates to the upper layers and thus the temperature of $MoTe_2$ increases. Second, due to the negative TECs of graphene and h-BN, the tension level of the whole suspended structure rises. To probe the temperature and strain level changes, Raman shifts and mechanical resonances are measured using the combined Raman and laser interferometry system (Supporting Information S1). Such a vdW heterostructure device shows clear resonances in moderate vacuum, with a fundamental-mode frequency $f \approx 14.7$ MHz (Figure 1d), demonstrating the heterostructure membrane is clearly suspended and vibrating. We also perform Raman measurements to characterize the device. From the Raman measurement results, characteristic peaks of $MoTe_2$ (Figure 1e),[22] graphene,[23] and h-BN[24] (Supporting Information S2) are observed. In particular, the phase of the $MoTe_2$ is confirmed as 2H after fabrication. It should be noted that the 2H A′ peak splits into two subpeaks, which is a unique Raman characteristic for few-layer 2H $MoTe_2$ samples.[22]

We then investigate the phase transition of sandwiched $MoTe_2$ sample by gradually increasing V_{DC}. **Figure 2** shows the Raman evolution of an 8-layer $MoTe_2$-based vdW device with voltage sweeping. For pristine $MoTe_2$ sample before Joule heating (V_{DC} = 0.0 V, Figure 2a), 2H E′ peak and 2H B′ peak are dominant, while in contrast, the 2H A′ peak is almost invisible. When the V_{DC} increases to 5.0 V, although the intensity of 2H E′, 2H B′, and 2H A′(L) peaks decrease, the 2H A′(R) peak becomes stronger (Supporting Information S4). Due to the anharmonic effect, the Stokes Raman peak intensity usually degrades with temperature elevation.[25] Therefore, the unusual intensity enhancement of 2H A′(R) suggests the appearance of new phase (1T′). Based on previously reported reversible $MoTe_2$ phase transition, the peak positions of 2H A′ mode (170–171 cm^{-1}) and 1T′ A_g (167–168 cm^{-1}) are very close,[20,26] and the redshift of 2H A′ peak results in its overlap with 1T′ A_g peak. When the voltage approaches 6.9 V, the 2H A′(L) disappears, and thus starting at this point, the peak around 165 cm^{-1} could be regarded as a pure 1T′ A_g peak. With voltage further increasing, the intensity of 1T′ A_g mode continuously grows while other 2H peaks degrade (2H E′ mode) even vanish (2H B′ and 2H A′ modes). These observations clearly demonstrate the 2H→1T′ phase transition. At 8.9 V, all 2H peaks disappear, indicating that the sample has completely transformed to 1T′ phase. It should be noted that another new peak, 1T′ D peak, appears at this point (V_{DC} = 8.9 V), with even higher intensity than the 1T′ A_g peak. The appearance of 1T′ D peak is related to the defect generation at high temperature.[27] With bias voltage increased to V_{DC} = 9.0 V, only 1T′ D peak remains, and A_g peak is invisible because of the strong anharmonic effect.

After the $MoTe_2$ has completely transformed to 1T′ phase, we gradually reduce the DC voltage (Figure 2b). Because device cooling is much slower than heating in vacuum, we always wait for 5 to 10 mins till the Raman signal is stabilized before further reducing the voltage. With the voltage decreased to 8.1 V, 1T′ A_g peak and 2H E′ peak appear, indicating the initialization of the reverse 1T′→2H phase transition. When the voltage is reduced to 7.0 V, both 1T′ A_g peak and 2H E′ peak become stronger compared with those at V_{DC} = 8.1 V, with, however, different reasons. The intensity increment of 1T′ A_g peak only results from decreasing temperature and thus reducing anharmonic effect. In contrast, the enhancement of 2H peak intensity is attributed to both reverse 1T′→2H phase transition and reducing anharmonic effect. This conclusion could be further supported by the trend when voltage drops from V_{DC} = 7.0 to 2.0 V. Due to the reversible phase transition, 1T′ A_g peak disappears completely while the 2H E′ peak becomes dominant. The vanishing of 1T′ peak shows the completion of reversible phase transition. When V_{DC} reduces to 0.0 V, as all the 2H peaks reappear and no 1T′ peak exists, $MoTe_2$ converts back to the original 2H pristine state completely, clearly demonstrating the $MoTe_2$ phase transition is a controllable and reversible process. To see the phase transition clearly, we extract and plot Raman peak intensity with voltage variation. The peak intensity ratio of 1T′ A_g peak over the sum of 1T′ A_g peak and 2H E′ peak is used to characterize the 1T′ ratio of the $MoTe_2$ sample during phase transition (Figure 2c,d). The approach to determining 1T′ peak intensity is described in Supporting Information S5.[20] It is noticed that there is a small phase transition hysteresis between the voltage increasing and decreasing branches, which might be attributed to the temperature variation hysteresis, that is, under the same voltage, there are still temperature differences between the voltage increasing and decreasing processes. Figure 2d shows the 1T′ ratio with voltage sweeping in a 14-layer $MoTe_2$-based vdW device (Device #2). The two devices exhibit a similar phase transition trend (the 1T′ ratios in these devices are determined from data in Supporting Information S3–S5).

Besides Raman peak intensity variation, another phenomenon during voltage sweeping is the Raman peak shift, that is, all Raman peaks redshift to the lower frequency regime and blueshift to higher frequency with temperature increases and decreases, respectively. The Raman peak position variation allows us to estimate the device temperature. The $MoTe_2$ and graphene temperature are calculated using the equation

$$\omega_T = \omega_{300K} + \chi(T - 300K) \quad (1)$$

where T is temperature, ω_T is Raman peak position at temperature T, ω_{300K} is Raman peak position at room temperature (300K), and χ is first-order temperature coefficient

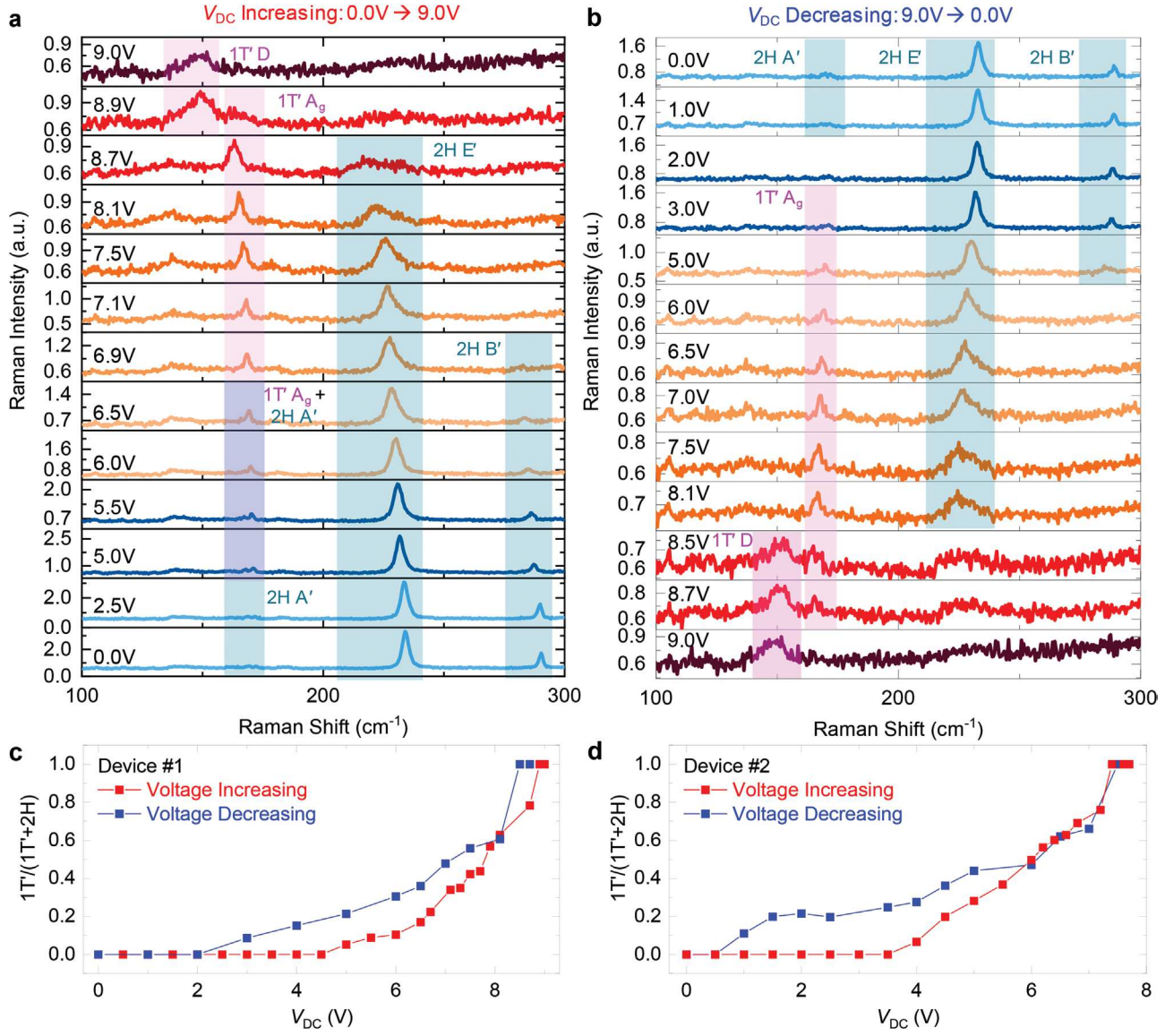

Figure 2. Evolution of Raman spectra measured during reversible phase transition in $MoTe_2$ vdW heterostructure devices. Evolution of $MoTe_2$ Raman spectra with voltage V_{DC} a) increasing and b) decreasing in an 8-layer $MoTe_2$-based vdW device. 1T′ phase ratio of $MoTe_2$ with the voltage sweeping in c) Device #1: an 8-layer $MoTe_2$-based vdW device and d) Device #2: a 14-layer $MoTe_2$-based vdW device.

(–0.015 cm^{-1} K^{-1} for graphene G peak[28] and –0.0164 cm^{-1} K^{-1} for $MoTe_2$ 2H E′ peak[29]). Because of the disappearance of the 2H peak E′ after $MoTe_2$ transitioning to 1T′, the 1T′ A_g peak position shift is used to calibrate temperature of the phase transition completion point (Supporting Information S6). **Figure 3** shows the measured lattice temperature of graphene and $MoTe_2$ at the device center region (Raman measurement spot) for two devices during reversible phase transition, tuned by applied bias voltage V_{DC}. For the 8-layer $MoTe_2$ device (Device #1, Figure 3a,b), the 2H→1T′ phase transition starts at 440 K (V_{DC} = 5.0 V). Above this point, two phases coexist together and 1T′ phase ratio keeps increasing. At around 1180 K (V_{DC} = 8.9 V), the $MoTe_2$ sample is fully converted to 1T′ phase. Because the phase transition completion temperature is very close to previously reported values (1200 K, purple dashed line in Figure 3[16,30]), tension does not play a crucial role in phase transition and phase transition is mainly driven by temperature change in Device #1. The temperature of graphene is 2000 K when V_{DC} = 8.9 V. This large temperature difference between graphene and $MoTe_2$ at this point could be explained by the significantly different thermal conductivity between graphene (5000 W/(m·K)[31]) and $MoTe_2$ (42 W/(m·K)[32]), and different interfacial thermal conductance between graphene/h-BN (52.2 MW/(m^2·K)[33]) and $MoTe_2$/h-BN (17.0 MW/(m^2·K)[33]). Considering that $MoTe_2$ and MoS_2 have very similar crystal structure, it is reasonable to speculate that interfacial thermal conductances at MoS_2/h-BN and $MoTe_2$/h-BN are similar. After the device has fully transformed into 1T′ phase, we reduce the applied voltage (Figure 3b). When the temperature is reduced to 925 K (V_{DC} = 8.1 V), the $MoTe_2$ flake starts to transition to 2H phase and this reversible phase transition process completes at 386 K (V_{DC} = 2.0 V). The phase transition of a 14-layer

$MoTe_2$ device (Device #2) is described in Figure 3c,d. The 2H to 1T′ phase transition process starts at 455 K and completes at 1050 K. Although two devices exhibit similar phase transition initialization temperature, the completion temperature in Device #2 (1050 K) is noticeably lower than the one in Device #1 (1180 K), suggesting that the other energy input (should be tension in this scenario) plays an important role in the phase transition in Device #2. The reversible phase transition (1T′ to 2H) starts at 810 K and completes at around 460 K.

In order to estimate the possible impact from the strain effect induced by Joule heating, we measure the resonance frequency under different V_{DC}, which allows us to extract the average thermal strain experienced by the heterostructure. The resonance frequency of the heterostructure can be written as follows

$$f = \frac{(k_2^{mn} na)}{2\pi}\sqrt{\frac{D}{\rho_{\text{Hetero}}\zeta a^4}\left[\frac{(\gamma_0+\gamma_{\text{th}})a^2}{D}+\left(k_2^{mn}a\right)^2\right]} \quad (2)$$

where $D=\frac{E_{\text{Y,Hetero}}t^3}{12(1-\nu^2)}$ is the flexural rigidity, ζ is coefficient of adsorbed mass, t is the total thickness of the heterostructure, γ_0 is the initial tension, and a is the radius of the microtrench.[34] $E_{\text{Y,Hetero}}$ and ρ_{Hetero} are effective Young's modulus and density of the heterostructure, which can be calculated as below

$$E_{\text{Y,Hetero}} = \frac{E_{\text{Y,Gr}}t_{\text{Gr}} + E_{\text{Y,BN}}(t_{\text{BN,bottom}} + t_{\text{BN,top}}) + E_{\text{Y,MoTe}_2}t_{\text{MoTe}_2}}{t_{\text{Gr}} + t_{\text{BN,bottom}} + t_{\text{BN,top}} + t_{\text{MoTe}_2}} \quad (3)$$

$$\rho_{\text{Hetero}}t_{\text{Hetero}} = \rho_{\text{Gr}}t_{\text{Gr}} + \rho_{\text{BN}}\left(t_{\text{BN,bottom}} + t_{\text{BN,top}}\right) + \rho_{\text{MoTe2}}t_{\text{MoTe2}} \quad (4)$$

Electrothermally induced tension (γ_{th}) can be obtained from measured frequency by using Equation 2. After obtaining electrothermally induced tension, we calculate the average thermal strain ($\varepsilon_{\text{th,avg}}$) experienced by the suspended heterostructure using the following equation

$$\varepsilon_{\text{th,avg}} = \frac{\gamma_{\text{th}}}{E_{\text{Y,Hetero}}t} \quad (5)$$

Figure 4a shows the measured resonance frequency f_{res} under increasing voltage for the 8-layer $MoTe_2$-based vdW device. With voltage V_{DC} increasing, due to the tension increase upon heating from the negative TECs of graphene and h-BN, the frequency of the device increases. It can be seen that in the low voltage regime (V_{DC} = 0 to 4 V), because the temperature does not increase significantly in this regime, the frequency is almost invariant with the applied voltage. From V_{DC} = 3.5 to 8.0 V, the frequency rises with applied voltage, which could be attributed to the significant temperature elevation (corresponding to $MoTe_2$ temperature increasing from 400 to 900 K).

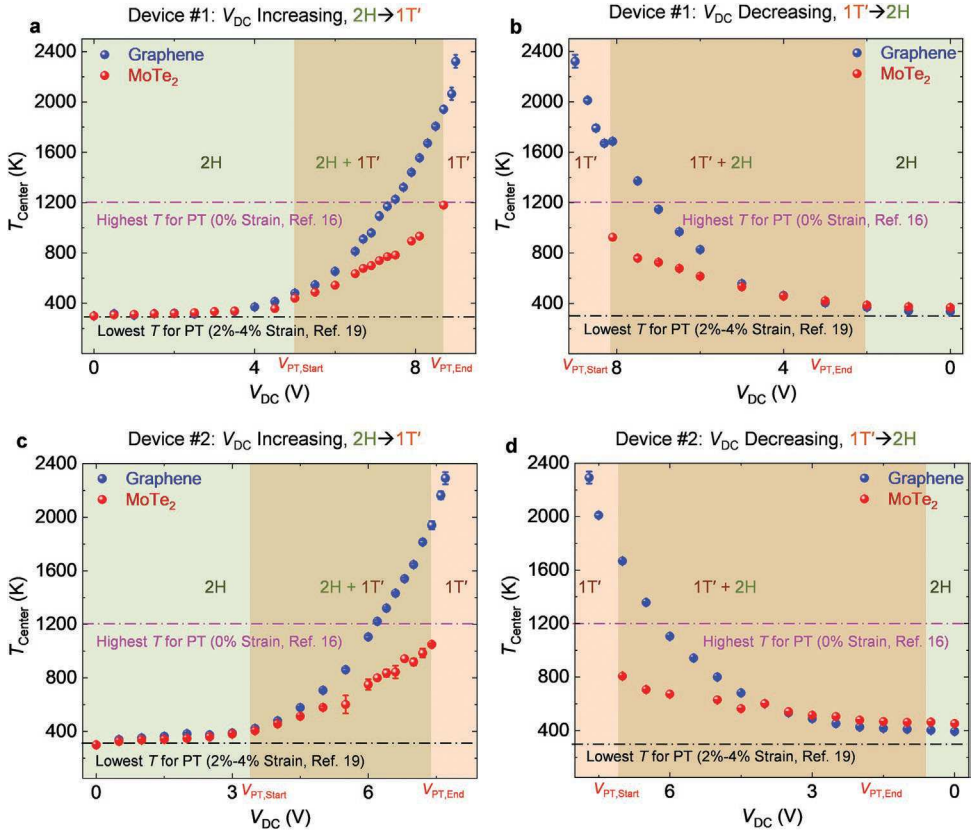

Figure 3. Temperature variation of $MoTe_2$ and graphene measured during reversible phase transition. Temperature a) increasing and b) decreasing of Device #1 (8-layer $MoTe_2$ device) with the DC voltage increasing and decreasing, respectively. Temperature c) increasing and d) decreasing of Device #2 (14-layer $MoTe_2$ device) with the DC voltage increasing and decreasing, respectively. The green, orange, and overlapped green/orange regions represent 2H phase, 1T′ phase, and 2H+1T′ mixed phase, respectively.

Beyond V_{DC} = 8.0 V, because of the transition from negative TECs to positive TECs of graphene and h-BN at high temperature (>1600 K),[35] the frequency decreases slowly with applied voltage. In the reversed (backward) phase transition process of Device #1, with the voltage decreasing from V_{DC} = 9.0 to 2.0 V, the frequency variation shows three regimes. In the first regime (from V_{DC} = 9.0 to 6.5 V), because of significant temperature lowering, the frequency decreases with applied voltage. In the second regime (V_{DC} = 6.5 to 4.0 V), the frequency shows an unusual gentle rise with voltage decreasing. One possible reason for this variation might be the formation and movement of tiny bubbles at the interfaces in the heterostructure (Supporting Information S8). In the third regime (V_{DC} = 4.0 to 2.0 V), the temperature effect becomes dominant again and frequency reduces with voltage decreasing. Utilizing the frequency variation results, we further extract the corresponding $\varepsilon_{th,avg}$, shown in Figure 4b, and we obtain that at the phase transition (2H to 1T′) completion point the thermal strain $\varepsilon_{th,avg}$≈ 0.055% for this Device #1. We notice that there is a tension difference (frequency difference) between the final state and initial state for Device #1. This difference could be attributed to the annealing effects or morphology change (wrinkles) at the interfaces in the device. Device #2 (Figure 4c,d) exhibits overall similar frequency variation trends as those in Device #1, but with two differences. First, the tension level of Device #2 at phase transition (2H to 1T′) completion point is $\varepsilon_{th,avg}$≈ 0.15%, much higher than that in Device #1, which is consistent with the fact that the phase transition temperature of Device #2 is much lower than that of Device #1. Second, the frequency and tension level of the initial state are close to those of the final state, demonstrating that there is no measurable morphology change (wrinkles) during the heating and cooling process.

With the temperature calibration and strain estimation, we plot the 1T′ ratio in 2H to 1T′ phase transition process versus coupled effects of MoT_2 lattice temperature and thermal strain (**Figure 5**). In Device #1 (Figure 5a), the phase transition begins at T_{MoTe2} = 440 K with a strain level around $\varepsilon_{th,avg}$ ≈ 0.01%. As the voltage V_{DC} increases, the temperature and thus thermal strain level elevates; consequently, the 1T′ phase ratio becomes increasingly dominant. When the temperature approaches T_{MoTe2} = 1180 K and a strain level around 0.055%, the $MoTe_2$ flake has completely transitioned to 1T′ phase. In Device #2 (Figure 5b), the 2H to 1T′ phase transition starts at T_{MoTe2} = 455 K, with tension level around $\varepsilon_{th,avg}$ ≈0.039%; and it completes at 1050 K with tension around 0.12%. The lower phase transition completion temperature in Device #2 is attributed to the relatively higher thermal tension induced by Joule heating.

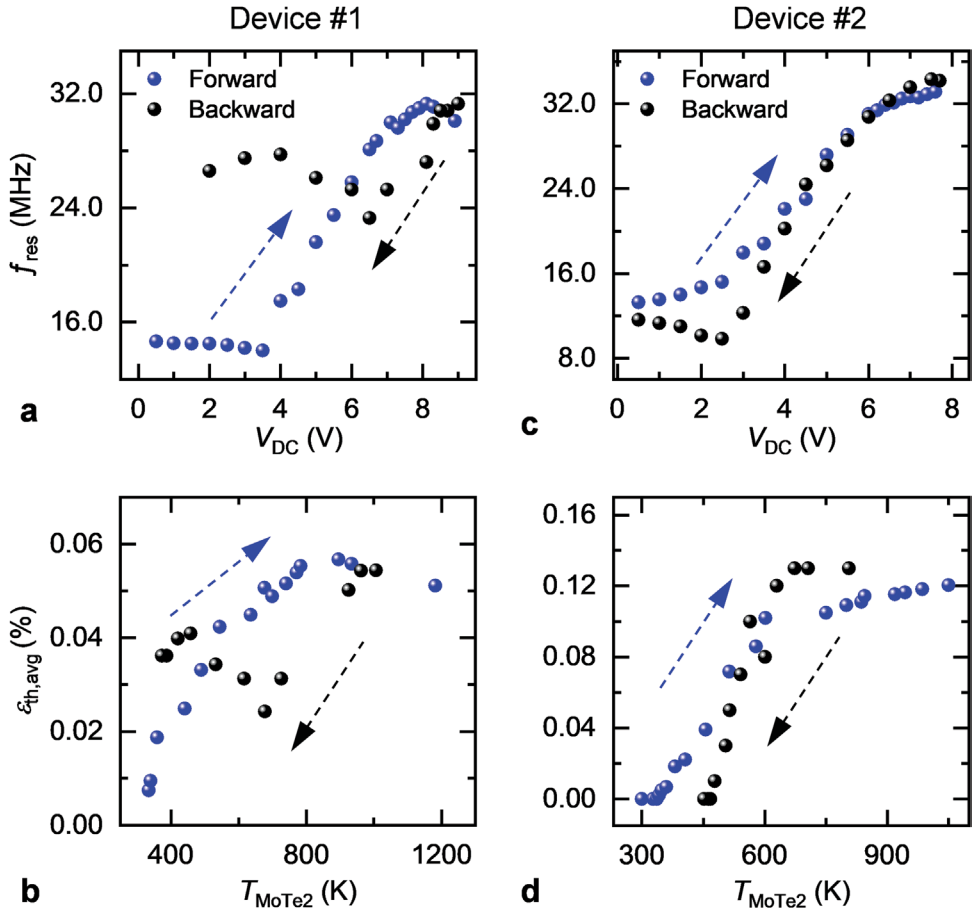

Figure 4. Frequency and strain evolutions measured for two $MoTe_2$-based vdW devices with varying voltage and temperature during the reversible phase transition. Frequency evolution of a) Device #1: an 8-layer $MoTe_2$ device and b) Device #2: a 14-layer $MoTe_2$ device with varying applied voltage. Thermal strain of c) Device #1 and d) Device #2 with varying temperature.

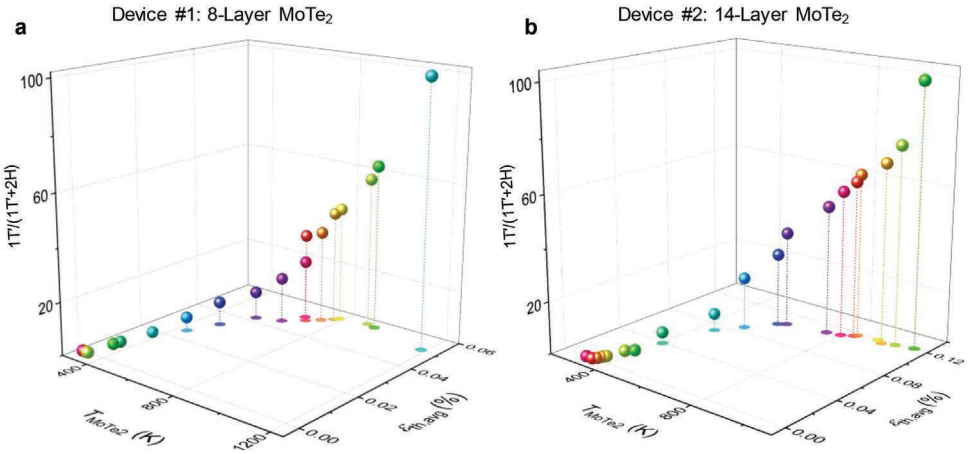

Figure 5. Coupled effects of varying temperature and strain in the 2H to 1T′ phase transition process in a) Device #1: an 8-layer $MoTe_2$-based vdW device and b) Device #2: a 14-layer $MoTe_2$-based vdW device.

3. Conclusions

In summary, we have demonstrated reversible and controllable $MoTe_2$ crystalline phase transition via electrothermal-mechanical tuning on a vdW heterostructure resonant nanoelectromechanical systems (NEMS) platform. By electrothermally heating the graphene nano-hotplate, the temperature of each layer in the vdW heterostructure and thus the thermal strain elevates. From measured Raman shift, we observe $MoTe_2$ transitions from 2H phase to 1T′ phase with rising temperature and strain level. In reverse, with voltage decreasing and thus temperature plus tension reducing, the 1T′ $MoTe_2$ converts back to 2H phase. The coexistence of 2H phase and 1T′ phase suggests that the $MoTe_2$ phase transition may be a gradual process. By monitoring the tension level from the resonance frequency, we find that tension could significantly lower the $MoTe_2$ phase transition completion temperature. This work demonstrates, for the first time, a novel platform for reversible $MoTe_2$ phase transition, with only two-terminal inputs needed, manufacturable on regular SiO_2-on-Si substrates. From an engineering perspective, this paves the way toward further integrating reversible $MoTe_2$ phase transition devices onto CMOS as it requires no other special substrates or additional components. This work opens a new avenue for designing and building phase transition $MoTe_2$ multiphysical devices that can capitalize on NEMS-enabled tuning and control, for memory and neuromorphic computing applications.

4. Experimental Section

Fabrication of Suspended Graphene/h-BN/$MoTe_2$/h-BN van der Waals Heterostructure: The bottom graphene flakes are first exfoliated from graphite crystals on PDMS and then transferred onto the pre-patterned microcavities on SiO_2-on-Si substrates using the all-dry transfer method.[21] Following the 1st transfer, bottom h-BN layer, $MoTe_2$ layer, and top h-BN layer are transferred on top subsequently, one by one. The bottom h-BN is employed to isolate graphene and $MoTe_2$, and the top h-BN is used to encapsulate $MoTe_2$ and prevent it from degradation. The diameter of the circular microtrench or microcavity is typically around 10 µm with a depth around 2.2 µm.

Raman Scattering Measurement: The graphene/h-BN/$MoTe_2$/h-BN vdW heterostructure devices are preserved in a vacuum chamber and measured using a custom-built micro-Raman spectrometer. The Raman spectrometer is integrated into an optical interferometric resonance measurement system (Figure S1, Supporting Information). In the Raman measurement, a 532 nm laser is focused upon the center of the vdW heterostructure. The spot size of laser is around ≈1 µm and the power of the 532 nm laser is lower than 200 µW. The electrical power applied to heat up graphene is 6 mW when graphene reaches 1200 K. The laser power is significantly lower than the electrical power applied.[36] Raman scattered light from the device is collected in backscattering geometry and then guided to the spectrometer (Horiba iHR550) with a 2400 g mm^{-1} grating. Raman signal is recorded using a liquid-nitrogen-cooled CCD.

Interferometric Resonance Measurement: The resonance characteristics of the vdW heterostructure devices are measured by an ultrasensitive optical interferometry system that we have built and meticulously engineered for systematically investigating 2D NEMS made of various 2D materials and their vdW heterostructures. The resonance motion is electrothermally excited by applying an RF signal v_{RF} coupled with a strong DC signal to drive the vdW heterostructure membrane. The resonance motion is detected by employing the same 532 nm green laser with power below 300 µW to avoid laser heating,[36] and the resonant motion-modulated optical interferometry signal is fed to a photodetector. A network analyzer is used to provide the sweeping RF drive signal, and to measure the resonance signal transduced by the photodetector.

Supporting Information

Supporting Information is available from the Wiley Online Library or from the author.

Acknowledgements

F.Y. and A.I. contributed equally to this work. The authors thank the support from the National Science Foundation (NSF) EPMD Award (Grants ECCS-1810154, ECCS-2015670 and ECCS-1809770) and CAREER Award (Grant ECCS-1454570, ECCS-2015708). Part of the device fabrication was performed at the Cornell Nanoscale Science and Technology Facility (CNF), a member of the National Nanotechnology Infrastructure Network (NNIN), supported by the National Science Foundation (Grant ECCS-1542081).

Conflict of Interest

The authors declare no conflict of interest.

Data Availability Statement

The data that support the findings of this study are available from the corresponding author upon reasonable request.

Keywords

2D materials, nanoelectromechanical systems, phase transition, van der Waal heterostructures

Received: August 29, 2022
Published online:

[1] A. Jo, W. Joo, W.-H. Jin, H. Nam, J. K. Kim, *Nat. Nanotechnol.* **2009**, *4*, 727.
[2] Y. Maeda, H. Andoh, I. Ikuta, H. Minemura, *J. Appl. Phys.* **1988**, *64*, 1715.
[3] M. Chen, K. A. Rubin, R. W. Barton, *Appl. Phys. Lett.* **1986**, *49*, 502.
[4] M. Wuttig, N. Yamada, *Nat. Mater.* **2007**, *6*, 824.
[5] C. Chen, A. Schrott, M. H. Lee, S. Raoux, Y. H. Shih, M. Breitwisch, F. H. Baumann, E. K. Lai, T. M. Shaw, P. Flaitz, R. Cheek, E. A. Joseph, S. H. Chen, B. Rajendran, H. L. Lung, C. Lam, in *Proc. of 2009 IEEE International Memory Workshop*, IEEE, Piscataway, NJ **2009**, pp. 1–2, https://doi.org/10.1109/IMW.2009.5090589.
[6] Q. Wang, B. Liu, Y. Xia, Y. Zheng, R. Huo, Q. Zhang, S. Song, Y. Cheng, Z. Song, S. Feng, *Appl. Phys. Lett.* **2015**, *107*, 222101.
[7] A. Schropp, J. Siegel, J. Solis, C. N. Afonso, M. Wuttig, in *Proc. of 2003 Conf. Lasers Electro-Optics Eur. (CLEO/Europe 2003) (IEEE Cat. No.03TH8666)*, IEEE, Piscataway, NJ **2003**, p. 748.
[8] M. Schumacher, H. Weber, P. Jóvári, Y. Tsuchiya, T. G. A. Youngs, I. Kaban, R. Mazzarello, *Sci. Rep.* **2016**, *6*, 27434.
[9] D. Kuzum, R. G. D. Jeyasingh, B. Lee, H.-S. P. Wong, *Nano Lett.* **2012**, *12*, 2179.
[10] T. Tuma, A. Pantazi, M. L. Gallo, A. Sebastian, E. Eleftheriou, *Nat. Nanotechnol.* **2016**, *11*, 693.
[11] K. F. Mak, C. Lee, J. Hone, J. Shan, T. F. Heinz, *Phys. Rev. Lett.* **2010**, *105*, 136805.
[12] C. Ruppert, O. B. Aslan, T. F. Heinz, *Nano Lett.* **2014**, *14*, 6231.
[13] J. Li, N. V. Medhekar, V. B. Shenoy, *J. Phys. Chem. C* **2013**, *117*, 15842.
[14] K.-A. N. Duerloo, Y. Li, E. J. Reed, *Nat. Commun.* **2014**, *5*, 4214.
[15] X. Qian, J. Liu, L. Fu, J. Li, *Science* **2014**, *346*, 1344.
[16] S. Song, D. H. Keum, S. Cho, D. Perello, Y. Kim, Y. H. Lee, *Nano Lett.* **2016**, *16*, 188.
[17] S. Cho, S. Kim, J. H. Kim, J. Zhao, J. Seok, D. H. Keum, J. Baik, D.-H. Choe, K. J. Chang, K. Suenaga, S. W. Kim, Y. H. Lee, H. Yang, *Science* **2015**, *349*, 625.
[18] Y. Tan, F. Luo, M. Zhu, X. Xu, Y. Ye, B. Li, G. Wang, W. Luo, X. Zheng, N. Wu, Y. Yu, S. Qin, X.-A. Zhang, *Nanoscale* **2018**, *10*, 19964.
[19] W. Hou, A. Azizimanesh, A. Sewaket, T. Peña, C. Watson, M. Liu, H. Askari, S. M. Wu, *Nat. Nanotechnol.* **2019**, *14*, 668.
[20] Y. Wang, J. Xiao, H. Zhu, Y. Li, Y. Alsaid, K. Y. Fong, Y. Zhou, S. Wang, W. Shi, Y. Wang, A. Zettl, E. J. Reed, X. Zhang, *Nature* **2017**, *550*, 487.
[21] R. Yang, X.-Q. Zheng, Z. Wang, C. J. Miller, P. X.-L. Feng, *J. Vac. Sci. Technol., B* **2014**, *32*, 061203.
[22] M. Grzeszczyk, K. Gołasa, M. Zinkiewicz, K. Nogajewski, M. R. Molas, M. Potemski, A. Wysmołek, A. Babiński, *2D Mater.* **2016**, *3*, 25010.
[23] A. C. Ferrari, J. C. Meyer, V. Scardaci, C. Casiraghi, M. Lazzeri, F. Mauri, S. Piscanec, D. Jiang, K. S. Novoselov, S. Roth, A. K. Geim, *Phys. Rev. Lett.* **2006**, *97*, 187401.
[24] X. Ling, W. Fang, Y.-H. Lee, P. T. Araujo, X. Zhang, J. F. Rodriguez-Nieva, Y. Lin, J. Zhang, J. Kong, M. S. Dresselhaus, *Nano Lett.* **2014**, *14*, 3033.
[25] G. Lucazeau, *J. Raman. Spectrosc.* **2003**, *34*, 478.
[26] D. Zakhidov, D. A. Rehn, E. J. Reed, A. Salleo, *ACS Nano* **2020**, *14*, 2894.
[27] Y. Yoo, Z. P. DeGregorio, Y. Su, S. J. Koester, J. E. Johns, *Adv. Mater.* **2017**, *29*, 1605461.
[28] I. Calizo, A. A. Balandin, W. Bao, F. Miao, C. N. Lau, *Nano Lett.* **2007**, *7*, 2645.
[29] H. Zhang, W. Zhou, X. Li, J. Xu, Y. Shi, B. Wang, F. Miao, *Appl. Phys. Lett.* **2016**, *108*, 091902.
[30] D. H. Keum, S. Cho, J. H. Kim, D.-H. Choe, H.-J. Sung, M. Kan, H. Kang, J.-Y. Hwang, S. W. Kim, H. Yang, K. J. Chang, Y. H. Lee, *Nat. Phys.* **2015**, *11*, 482.
[31] A. A. Balandin, S. Ghosh, W. Bao, I. Calizo, D. Teweldebrhan, F. Miao, C. N. Lau, *Nano Lett.* **2008**, *8*, 902.
[32] A. Shafique, Y.-H. Shin, *Phys. Chem. Chem. Phys.* **2017**, *19*, 32072.
[33] Y. Liu, Z.-Y. Ong, J. Wu, Y. Zhao, K. Watanabe, T. Taniguchi, D. Chi, G. Zhang, J. T. L. Thong, C.-W. Qiu, K. Hippalgaonkar, *Sci. Rep.* **2017**, *7*, 43886.
[34] F. Ye, J. Lee, P. X.-L. Feng, *Nanoscale* **2017**, *9*, 18208.
[35] F. Ye, J. Lee, P. X.-L. Feng, in *Proc. of IEEE International Electron Devices Meeting (IEDM)*, IEEE, Piscataway, NJ **2018**, pp. 87–90, https://doi.org/10.1109/IEDM.2018.8614604.
[36] F. Ye, J. Lee, P. X.-L. Feng, *Nano Lett.* **2018**, *18*, 1678.